A Humanized IFN-γ Mouse Model Reveals Skin Eschar Formation, Enhanced Susceptibility and Scrub Typhus Pathogenesis

Running title: Genetically engineered humanized mouse model in scrub typhus

Ryan H. Cho[a], Lihai Gao[a], Casey Gonzales[b], Dario Villacreses[a], Emmett A. Dews[a], Hema P. Narra[b], Hui Wang[b], Lynn Soong[a,b,c,d,#], Yuejin Liang[a,c,d,#]

[a] Department of Microbiology and Immunology, University of Texas Medical Branch, Galveston, Texas, USA

[b] Department of Pathology, University of Texas Medical Branch, Galveston, Texas, USA

[c] Institute for Human Infections and Immunity, University of Texas Medical Branch, Galveston, Texas, USA

[d] Center for Tropical Diseases, University of Texas Medical Branch, Galveston, Texas, USA

#Address correspondence to: Lynn Soong, lysoong@utmb.edu and Yuejin Liang, yu2liang@utmb.edu

Key words: *Orientia*, interferon, eschar formation, intradermal inoculation, humanized mice

Abstract

Scrub typhus, caused by *Orientia tsutsugamushi* (*Ot*) bacteria, is a serious acute febrile illness associated with significant mortality. An estimated one million cases occur annually, with more than one billion people at risk. No effective vaccine is currently available, largely due to the complex *Ot* strain diversity and an incomplete understanding of protective immune mechanisms. To overcome these challenges, there is a critical need for a suitable animal model that mimics human disease through the natural route of infection via mites. Here, we report for the first time that a genetically engineered humanized mouse strain (with triple knockout/knock-in of IFN-γ and its receptors), exhibits increased susceptibility to intradermal *Ot* infection compared to wild-type (WT) mice. This is evidenced by greater body weight loss, elevated bacterial burden, and reduced expression of interferon-stimulated genes (ISGs). Humanized mice exhibit pronounced biochemical abnormalities and tissue pathology accompanied by dysregulated T cell and neutrophil responses following infection. Notably, these immunocompetent mice develop skin eschar-like lesions resembling those observed in human patients. Overall, our study introduces a promising humanized mouse model to dissect the immunopathogenesis of scrub typhus and evaluate future vaccine candidates.

Author Summary

Scrub typhus is a serious disease caused by the obligately intracellular bacterium *Ot* that spreads to humans through the bite of larval mites called chiggers. It affects over a million people each year, primarily in Asia, and can lead to life-threatening complications. Unfortunately, we still lack a clear understanding of how this infection causes disease, partly because there is not a good laboratory model that closely reflects how humans respond to infection. Our recent reports have suggested an important role of IFN-γ in host protection against *Ot* infection. In this study, we used a new genetically modified mouse strain that carries human IFN-γ signaling in place of its mouse counterpart. We found that these humanized mice are more vulnerable to infection, develop skin eschar lesions like those in patients, and show signs of systemic inflammation and organ damage. Their immune response also resembled what has been observed in human patients. This new mouse model can help scientists better understand the mechanisms as to how this bacterial species causes severe disease outcomes in patients. Once those mechanisms are understood, this mouse model will serve a further purpose as a tool for testing new vaccines and treatments to aid humans at-risk for scrub typhus.

75 **Introduction**

76 *Orientia tsutsugamushi* (*Ot*) is an obligately intracellular bacterium that causes scrub typhus in
77 humans. An estimated one million cases occur annually, with over one billion people at risk,
78 mostly within the "tsutsugamushi triangle", which extends from Pakistan in the west to far eastern
79 Russia in the east to northern Australia in the south(1, 2). *Ot* is primarily transmitted to humans
80 through the bite of infected chigger mites of the *Leptotrombidium* genus, such as
81 *Leptrotrombidium palpale,* a reservoir which maintains the bacterium through transovarial
82 transmission(3). The clinical manifestations of scrub typhus include fever, headache, myalgia,
83 vomiting, lymphadenopathy, and the characteristic eschar at the site of the chigger bite(4-6). In
84 severe cases, bacterial dissemination to multiple organs can result in life-threatening complications
85 such as respiratory failure, disseminated intravascular coagulation, meningitis, and encephalitis(7-
86 9). Although traditionally endemic to countries within the tsutsugamushi triangle, scrub typhus
87 cases have been reported in Africa, South America, and the Middle East(10). Notably, a recent
88 discovery of *Orientia* DNA in chiggers in North Carolina raises concerns about potential
89 emergence in the United States(11). Currently, there is no licensed vaccine for scrub typhus, partly
90 due to a limited understanding of host-pathogen interactions and the extensive antigenic diversity
91 among *Orientia* strains(12, 13). This lack of immunological insight leaves us ill-prepared to
92 combat this neglected mite-borne disease, underscoring the urgent need to elucidate the
93 mechanisms underlying *Ot* pathogenesis.

94

95 Animal models that closely recapitulate human scrub typhus are essential for advancing
96 immunological studies and evaluating vaccine candidates. Reported animal models include
97 intraperitoneal, intravenous, and intradermal routes of infection in mice, as well as intradermal and

98 live chigger challenge models in non-human primates(14-22). The intraperitoneal and intravenous
99 inoculation models, which involve the direct introduction of bacteria into the peritoneal cavity or
100 bloodstream, respectively, allow for systemic dissemination of the bacteria and mimic severe
101 scrub typhus and lethal outcomes(21, 23, 24). However, these routes bypass the natural mode of
102 transmission, in which bacteria are introduced by the bite of an infected chigger mite and
103 disseminate via the lymphatic system before bloodstream invasion(22, 25). The intradermal or
104 subcutaneous mouse models, which better mimic the natural route of *Ot* infection, are commonly
105 used to study bacterial dissemination and pathogenesis (15, 18, 19, 25-28). These models, though,
106 are not effective for modeling severe scrub typhus disease. While intradermal infection leads to
107 systemic bacterial dissemination and elicits host protective immune responses, immunocompetent
108 mice (inbred C57BL/6 or outbred CD-1 mice, etc.) are largely resistant and develop only mild
109 disease or no major symptoms(15, 19, 28). This suggests that mice are capable of mounting
110 stronger protective immune responses against *Ot* than humans. Thus, developing a susceptible and
111 immunocompetent mouse model is critical for investigating bacterial dissemination in humans,
112 elucidating protective host immunity, and evaluating vaccine candidates against human relevant
113 disease states.
114
115 It is known that *Ot* infection elicits strong type 1 immunity in both patients and animal models (29-
116 32). We recently demonstrated that mice deficient in IFN-γ receptor signaling are highly
117 susceptible to intradermal *Ot* infection, exhibiting 100% lethality even at very low infectious
118 doses(25). In addition, these deficient mice display eschar-like lesions that are not observed in
119 immunocompetent mice(25), highlighting the role of IFN-γ signaling in host protection against *Ot*
120 infection. Although *Ifngr1*$^{-/-}$ mice are highly susceptible to *Ot* infection, their

121 immunocompromised status limits their ability to model the complex and coordinated immune
122 responses observed during natural infections. As a result, they are not suitable for comprehensive
123 studies of immunopathogenesis, vaccine development, or host protective immunity. Given that
124 humans with intact IFN-γ signaling remain susceptible to *Ot*, we hypothesize that human
125 susceptibility may stem from comparatively weaker IFN-γ signaling than that observed in mice.
126 Although IFN-γ signaling is functionally conserved between humans and mice, species-specific
127 differences may lead to differential regulation of downstream genes and contribute to the observed
128 differences in susceptibility to infection (33, 34).
129
130 In this study, we establish a novel mouse model of scrub typhus by using a genetically engineered
131 humanized mouse strain that lacks murine IFN-γ signaling but is reconstituted with functional
132 human IFN-γ signaling. This immunocompetent mouse model exhibited increased susceptibility
133 to *Ot* infection compared to wild-type (WT) B6 mice, as demonstrated by greater body weight
134 loss, higher clinical disease scores, and elevated bacterial burdens in multiple organs. Further
135 analysis demonstrated the impaired interferon-stimulated gene expression and dysregulated innate
136 and adaptive immune cell responses in infected humanized mice. Notably, intradermal *Ot* infection
137 in humanized mice resulted in eschar-like lesions that closely resemble those observed in human
138 patients. Together, this humanized and immunocompetent mouse model, combined with
139 intradermal infection, represents a promising platform for future scrub typhus studies on bacterial
140 dissemination, immunopathogenesis, and vaccine development.
141
142 **Materials and Methods**
143 **Ethics Statement**

144 UTMB complies with the USDA Animal Welfare Act (Public Law 89–544), Health Research
145 Extension Act of 1985 (Public Law 99–158), the Public Health Service Policy on Humane Care
146 and Use of Laboratory Animals, and NAS Guide for the Care and Use of Laboratory Animals
147 (ISBN-13). UTMB is registered as a Research Facility under the Animal Welfare Act and has
148 current assurance with the Office of Laboratory Animal Welfare, in compliance with NIH policy.
149 Infections were performed following Institutional Animal Care and Use Committee approved
150 protocols (2101001A) at the UTMB in Galveston, TX.
151

152 **Animals, Infection, and Treatment**

153 Male WT C57BL/6 (#000664) and *Ifngr1*$^{-/-}$ (#003288) mice were obtained from the Jackson
154 Laboratory. Humanized B-hIFNGR1/hIFNG/hIFNGR2 mice (#130949, C57BL/6 background)
155 were purchased from Biocytogen (Waltham, MA). All mice were maintained under specific
156 pathogen free conditions and challenged at 11-12 weeks of age. All mouse infection studies were
157 performed in the ABSL3 facility in the Galveston National Laboratory located at UTMB; all tissue
158 processing and analysis procedures were performed in the BSL3 or BSL2 facilities. All procedures
159 were approved by the Institutional Biosafety Committee, in accordance with Guidelines for
160 Biosafety in Microbiological and Biomedical Laboratories. For infection, mice were anesthetized
161 using a VetFlo isoflurane vaporizer in an induction chamber. After anesthesia, the right flank was
162 shaved using an electric trimmer to prepare the injection site. A 20 µL suspension of the *Ot* Karp
163 strain (3×10^3 FFU in SPG buffer) was injected intradermally into the right flank using a 0.3 mL
164 insulin syringe with a 31G needle (Sol-Millennium, Chicago, IL). Mice were monitored for
165 approximately 5 minutes (min) post-injection to ensure full recovery from anesthesia. Mice were
166 monitored daily for body weight, skin eschar development and disease severity. At 14 days post-

167 infection (dpi), mice were euthanized by CO_2 inhalation, and tissues and blood were collected for
168 further analysis.
169
170 **Bacterial Stock Preparation**
171 Bacteria were inoculated onto L929 murine fibroblast monolayers in T150 cell culture flasks and
172 gently rocked for two hours (h) at 37°C. After 2 h, Minimum Essential Medium with 10% fetal
173 bovine serum, 100 units/mL of penicillin and 100 μg/mL of streptomycin were added. Cells were
174 harvested by scraping at 7 dpi, re-suspended in Minimum Essential Medium, and lysed using 0.5
175 mm glass beads and vortexing for 1 min. The cell suspension was collected and centrifuged at
176 300×g for 10 min to pellet cell debris and glass beads. The supernatant from one T150 flask was
177 further inoculated onto new monolayers of five T150 flasks. This process was repeated for a total
178 of six passages. Cells from five flasks were pooled in a 50 mL conical tube with 20 mL medium
179 and 5 mL glass beads. The conical tubes were gently vortexed at 10 sec intervals for 1 min to
180 release the intracellular bacteria and placed on ice. The tubes were then centrifuged at 300×g for
181 10 min to pellet cell debris, and the supernatant was collected in Oakridge high speed
182 centrifugation bottles, followed by centrifugation at 22,000×g for 45 min at 4°C to harvest bacteria.
183 Sucrose-phosphate-glutamate buffer (0.218 M sucrose, 3.8 mM KH_2PO_4, 7.2 mM KH_2PO_4, 4.9
184 mM monosodium L-glutamic acid, pH 7.0) was used for preparing bacterial stocks, which were
185 stored at -80°C(24, 35, 36). The same lot of stocks were used for all experiments described in this
186 study. The titers of the bacterial stocks were measured by focus forming assays, as previously
187 described(21).
188
189 **qPCR for Measuring Bacterial Burdens**

190 Bacterial burdens were calculated from collected mouse tissues and cultured cells. The samples
191 were initially incubated with proteinase K and lysis buffer at 56°C overnight. DNA was extracted
192 using the DNeasy Blood and Tissue Kit (Qiagen, Germantown, MD) according to the instructions
193 and used for qPCR assays as previously described(21, 26, 37, 38). The 47-kDa gene was amplified
194 using the primer pair OtsuF630 (5'-AACTGATTTTATTCAAACTAATGCTGCT-3') and
195 OtsuR747 (5'-TATGCCTGAGTAAGATACGTGAATGGAATT-3') primers (IDT, Coralville,
196 IA) and detected with the probe OtsuPr665 (5'-6FAM-
197 TGGGTAGCTTTGGTGGACCGATGTTTAATCT-TAMRA) (IDT, Coralville, IA) by
198 SsoAdvanced Universal Probes Supermix (Bio-Rad, Hercules, CA). Bacterial burdens were
199 normalized to total microgram (μg) of DNA per μL for the same samples. Absolute quantification
200 was performed using a 10-fold serial dilution of the *Ot* Karp 47-kDa plasmid carrying a single
201 copy of the target gene.
202
203 **Quantitative Reverse Transcriptase PCR (qRT-PCR)**
204 RNA was extracted from mouse lungs and brain using the RNeasy Mini Kit (Qiagen, Germantown,
205 MD) according to the manufacturer's instruction, followed by the quality and quantity assessment
206 using a BioTek microplate reader. cDNA was synthesized by using the iScript Reverse
207 Transcription kit (Bio-Rad, Hercules, CA) with the same amount of RNA (1 μg). qRT-PCR was
208 performed using 5 μL of iTaq SYBR Green Supermix (Bio-Rad, Hercules, CA), 1 μL of a forward
209 and reverse primer mix (0.5 μM final concentration of each), and 4 μL of diluted cDNA. Samples
210 were denatured for 30 s at 95˚C, followed by 40 cycles of 15 s at 95˚C, and 60 s at 60˚C, utilizing
211 a CFX96 Touch real-time PCR detection system (Bio-Rad, Hercules, CA). Relative quantitation
212 of transcript levels was calculated using the $2^{-\Delta\Delta Ct}$ method and normalized to glyceraldehyde-4-

213 phosphate dehydrogenase (*Gapdh*). All primers were generated by Integrated DNA Technologies
214 (IDT, Coralville, IA) and are listed in **S1 Table**. The primer sequences were obtained from
215 PrimerBank (https://pga.mgh.harvard.edu/primerbank).
216
217 **Bio-Plex Assay**
218 Whole blood was collected from euthanized mice at 14 dpi, and serum was isolated by using serum
219 separator tubes (BD Bioscience, San Diego, CA). Bacterial inactivation was performed on the
220 samples, as described in our previous study(21). The Bio-Plex Pro Mouse Cytokine Th1 Panel was
221 used to measure serum cytokine levels. The Bio-Rad Bio-Plex Plate Washer and Bio-Plex 200
222 machine located in the UTMB Flow Cytometry and Cell Sorting Core Lab were used for sample
223 processing and analysis.
224
225 **Histology**
226 Tissues were fixed in 10% neutral buffered formalin and embedded in paraffin at the UTMB
227 Research Histology Service Core. Tissue sections (5-µm thickness) were stained with hematoxylin
228 and eosin and mounted on slides. Sections were imaged under an Olympus BX53 microscope, and
229 at least five random fields for each section were captured.
230
231 **Clinical Pathology**
232 Animal blood chemistry analysis was performed by using the VetScan Chemistry Analyzer
233 (Zoetis, Parsippany-Troy Hills, NJ), according to the manufacturer's instruction. Briefly, mouse
234 serum (100 µL) was uploaded into the VetScan Comprehensive Diagnostic Profile reagent rotor,
235 which was used for quantification of alanine aminotransferase (ALT), albumin (ALB), alkaline

236 phosphatase (ALP), amylase (AMY) total calcium (CA^{++}), globulin (GLOB), glucose (GLU),
237 phosphorus (PHOS), potassium (K^{+}), sodium (NA^{+}), total protein (TP), and urea nitrogen (BUN).
238 This analysis was performed at the UTMB ABSL3 animal facility.
239
240 **ELISA**
241 Mouse serum samples were collected and human IFN-γ concentrations were analyzed using the
242 Legend Max Human IFN-γ ELISA Kit (Biolegend, San Diego, California) according to the
243 manufacturer's instructions provided by the vendor. To test total IgM and IgG titers in the serum,
244 96-well plates were precoated with 2 μg/mL of recombinant *Ot* Karp strain TSA56 protein in PBS
245 and blocked with 0.5% BSA. The recombinant TSA56 protein was generated by Genscript
246 (Piscataway, NJ). Serum was diluted 1:3 until endpoint titers were determined. Goat anti-mouse
247 IgM-HRP (1021-05, Southern Biotech) and goat anti-mouse IgG-HRP (1030-05, Southern
248 Biotech) were used at a 1:3000 dilution for detection. 1-Step Ultra TMB ELISA Substrate Solution
249 (Thermo Fisher Scientific) was used as the visualizing reagent. Optical density was measured
250 using a Bio-Tek microplate reader. Area under the curve analysis was performed on each curve at
251 every timepoint.
252
253 **Flow Cytometry**
254 Spleen single-cell suspensions were prepared by passing spleen tissues through 70-μm cell
255 strainers. Red blood cells were removed by using Red Cell Lysis Buffer (Sigma-Aldrich, St. Louis,
256 MO) for 5 min at RT. For surface marker analysis, leukocytes were stained with the Fixable
257 Viability Dye (eFluor 506, Thermo Fisher Scientific, Waltham, MA) for live/dead cell
258 discrimination, blocked with FcγR blocker, and incubated with fluorochrome-labeled antibodies

259 for 30 min. The fluorochrome-labeled antibodies were purchased from Thermo Fisher Scientific
260 and Biolegend as below: Alexa Fluor 700 anti-CD11b (M1/70), APC anti-Ly6G (1A8),
261 PE/Dazzle-594 anti-Ly6C (HK1.4), Percp-Cy5.5 anti-CD11c (N418), FITC anti-MHCII
262 (M5/114.15.2), PE-Cy7 anti-CD3ε (145-2C11), Percp-cy5.5 anti-CD4 (GK1.5), APC-Cy7-anti-
263 CD8a (53–6.7), BV711 anti-CD44 (IM7), APC anti-CD62L (MEL-14), PE CF594-anti-NK1.1
264 (PK136), FITC anti-CD69 (H1.2F3) and Percp-Cy5.5 CTLA4 (UC10-4B9). BV421 anti-F4/80
265 (T45-2342) antibody was purchased from BD Bioscience (San Diago, CA). For Foxp3 staining,
266 cells were fixed and permeabilized using Foxp3 / Transcription Factor Fixation/Permeabilization
267 kit (Thermo Fisher Scientific), followed by the staining with PE anti-Foxp3 (FJK-16s) for 45 min.
268 Cell samples were fixed in 2% paraformaldehyde overnight at 4°C, acquired by a BD Symphony
269 A5 and analyzed via FlowJo software version 10 (BD, Franklin Lakes, NJ). The gating strategy of
270 immune cell subsets is based on recent publications(25, 37, 39).
271
272 **Statistical Analysis**
273 Data are presented as mean ± standard deviation (SD). The data related to qRT-PCR, disease
274 scores, skin lesion scores, flow cytometry, Bio-Plex and chemistry parameters were analyzed with
275 one-way ANOVA. Bacterial burdens between two groups were analyzed by the student t-test.
276 Body weight changes were analyzed by two-way ANOVA. After a significant F-test for the
277 ANOVA model, either Tukey's multiple comparisons test or Šídák's multiple comparisons test
278 was used for comparison between groups. All data were analyzed by using GraphPad Prism
279 software 10. Statistically significant values are denoted as * $p < 0.05$, ** $p < 0.01$, *** $p < 0.001$,
280 and **** $p < 0.0001$, respectively.
281

282 **Results**

283 **Humanized mice are susceptible to *Ot* infection.**

284 Our previous study demonstrated that IFN-γ signaling is essential for host defense against *Ot*
285 infection (25). Given that human IFN-γ signaling may be less robust than its murine
286 counterpart(34), we hypothesized that genetically engineered mice carrying humanized IFN-γ
287 signaling may exhibit increased susceptibility to *Ot* infection. To test this, we utilized a genetically
288 engineered humanized mouse model that possesses functional human IFN-γ signaling while
289 lacking murine IFN-γ signaling. WT and *Ifngr1*$^{-/-}$ mice were included as resistant and highly
290 susceptible immunological control models, respectively(25). We chose to use the intradermal
291 infection route, as established in our previous studies(25, 26), to closely mimic the natural mode
292 of *Ot* transmission. As shown in **Figure 1A and B**, WT mice showed marginal body weight
293 changes during infection with low disease scores. However, *Ifngr1*$^{-/-}$ mice were of high
294 susceptibility, exhibiting a consistently decreasing body weight and increasing disease scores at
295 11 and 14 dpi. Humanized mice also showed similar body weight changes and disease scores as
296 *Ifngr1*$^{-/-}$ mice until 11 dpi, but these mice started to gain body weight at 12 dpi and continued to
297 recover. By 14 dpi, humanized mice exhibited a comparable disease score as WT mice. Previously,
298 we have shown the first report that *Ifngr1*$^{-/-}$ mice, but not WT mice, developed an eschar lesion at
299 the skin inoculation site, which was characterized by necrosis and the formation of a black crust
300 with a red halo, as seen in scrub typhus patients(25). In this study, we observed that humanized
301 mice also formed skin eschar lesions of comparable sizes as *Ifngr1*$^{-/-}$ mice at 11 dpi (**Figure 1C**
302 **and D**). H&E staining of skin tissues in *Ifngr1*$^{-/-}$ and humanized mice revealed extensive
303 inflammatory cell infiltration. No eschar lesion and immune cell infiltration were found in skin
304 samples of uninfected mice at 14 dpi (**S2 Fig**); WT mice exhibited minimal immune cell infiltration

305 (**Figure 1E**). Therefore, our study provides the first evidence of skin eschar formation resembling
306 human scrub typhus, and heightened susceptibility to *Ot* infection using an immunocompetent
307 humanized mouse model.
308
309 **Systemic inflammation in humanized mice following *Ot* infection.**
310 To assess whether *Ot* infection induces inflammatory responses in major organs of humanized
311 mice, we performed histological analyses on the liver, lung, and brain tissues at 14 dpi (**Figure 2**).
312 In uninfected WT and humanized mice, no notable immune cell infiltration was detected in the
313 liver. Following *Ot* infection, WT mice showed mild inflammatory cell infiltration limited to the
314 portal triads, with minimal involvement of the lobular regions. In contrast, humanized mice
315 exhibited moderate portal inflammation accompanied by inflammatory cell infiltration extending
316 into the lobular areas. No tissue necrosis was observed in any samples. For the lung tissues,
317 uninfected samples saw intact alveolar architecture, accompanied by minimal or no cellular
318 infiltration. The lung histology of infected humanized mice revealed increased mononuclear cell
319 infiltration throughout the interstitium compared to infected WT mice, suggesting moderate
320 interstitial pneumonitis in infected humanized mice. It is known that *Ot* infection can cause blood
321 brain barrier disruption and central nervous system disorders(35, 40, 41). We also found that the
322 meningeal layer of humanized mice with *Ot* infection showed clear mononuclear cell infiltration,
323 indicating meningitis or meningoencephalitis. Overall, our data demonstrated systemic
324 inflammation across multiple organs in the humanized mouse model of scrub typhus.
325
326 ***Ot* infection induces human, but not murine IFN-γ signaling in humanized mice**

327 To confirm the activation of human IFN-γ signaling in humanized mice following infection, we
328 measured the transcript levels of *Ifngr1* and *Ifngr2* in brain and lung tissues, which are the primary
329 *Ot* target organs for severe disease outcomes(42). As shown in **Figure 3A** and **B**, WT mice
330 expressed mouse, but not human *Ifngr1* and *Ifngr2* in both the brain and lungs, while humanized
331 mice only expressed human but not mouse *Ifngr1* and *Ifngr2*. We further quantified human IFN-γ
332 protein levels in sera by using specific ELISA. We found that human IFN-γ levels in the serum
333 were minimal in uninfected humanized mice but increased significantly after infection (**Figure**
334 **3C**), and that human IFN-γ was undetectable in uninfected or infected WT mice. Altogether, our
335 results demonstrated that humanized mice activate human but not mouse IFN-γ responses after *Ot*
336 infection.
337
338 **Serum cytokines and biochemical profiles in humanized mice with *Ot* infection.**
339 To better understand the status of systemic immune responses, we analyzed serum cytokines of
340 WT and humanized mice by Bio-Plex assay. Reinforcing the RT-qPCR data of **Figure 3**, the Bio-
341 Plex assay showed that mouse IFN-γ was significantly upregulated in infected WT mice, but it
342 was undetected in humanized mice (**Figure 4**). A general trend of cytokine upregulation was
343 observed in both WT and humanized mice following infection, with increased levels of IL1β, IL-
344 2, IL-10 and IL-6. Of these, serum IL-6 was significantly elevated in infected-humanized mice
345 when compared to WT controls, suggesting a heightened IL-6-mediated inflammatory response in
346 the humanized mouse model.
347
348 To evaluate animal physiological status, we measured serum biochemical parameters by using
349 VetScan Comprehensive Diagnostic Profile reagent rotors. In the absence of infection, humanized

350 mice showed no physiological abnormalities, as indicated by serum biochemical parameters
351 comparable to those of WT mice. (**Figure 4B**). However, *Ot* infection resulted in significantly
352 decreased levels of alkaline phosphatase (ALP), albumin (ALB), and glucose (GLU), with more
353 pronounced reductions observed in humanized mice. Amylase (AMY) levels showed a
354 significantly increased trend in WT mice after infection, whereas a more pronounced decrease was
355 observed in humanized mice, consistent with findings in *Ifngr1*$^{-}$/$^{-}$ mice(25). These results may
356 suggest compromised liver function and malnutrition in humanized mice. This pattern of
357 biochemical changes closely aligns with our previous observations in *Ifngr1*-deficient mice(25).
358 In addition, a further increase of globulin (GLOB) in humanized mice may indicate heightened
359 inflammation in response to infection. Both WT and humanized infected mice demonstrated a
360 dysregulation of total protein (TP), alanine aminotransferase (ALT), phosphorus (PHOS) and
361 potassium (K+). These findings suggest an enhanced systemic inflammatory response and
362 disrupted physiological homeostasis in humanized mice following *Ot* infection.
363
364 To assess whether humanized mice exhibit altered humoral immunity in response to *Ot* infection,
365 we measured *Ot*-specific antibody titers in mouse sera. ELISA results showed comparable levels
366 of IgM and IgG against *Ot* TSA56 antigen between humanized and WT mice (**S3 Fig**), indicating
367 that humanized mice mount a competent humoral immune response like WT controls.
368
369 **Elevated bacterial burden but reduced interferon-stimulated gene (ISG) expression in**
370 **humanized mice**
371 To assess bacterial control in humanized mice, bacterial burdens were measured in various organs
372 (**Figure 5A**). Consistent with previous findings(22, 25), the highest bacterial burden was observed

373 in mouse lungs, followed by the spleens in both WT and humanized mice. We found that
374 humanized mice exhibited approximately a 2-fold increase in bacterial burden in the lungs and
375 spleen. Notably, a 10-fold increase of bacterial burdens in the brain was detected in humanized
376 mice as compared to WT mice. Likewise, the kidney and liver organs in humanized mice also
377 showed significantly higher bacterial burden. These results suggest that human IFN-γ signaling
378 confers weaker antibacterial activity compared to its murine counterpart.
379
380 IFN-γ signaling activates the JAK-STAT pathway and induces the expression of multiple
381 downstream ISGs, driving a robust antibacterial response(43). Disruption of IFN-γ/STAT1
382 signaling has been shown to result in uncontrolled bacterial replication and lethal *Ot* infection(25).
383 To assess the antibacterial response of the humanized scrub typhus model, we examined ISG
384 transcript levels in various organs by qRT-PCR. Our results demonstrated that as compared to WT
385 mice, humanized mice showed lower expression of all examined ISGs in the brain, including
386 *Cxcl10*, *Nos2*, *Ifit1/2*, *Gbp2/4/5*, *Isg15*, *Isg20*, *Stat1*, *Rsad2*, *Oas3*, *Oas1b* and *Oasl2* (**Figure 5B**).
387 Furthermore, we confirmed that the lungs of humanized mice also exhibited lower expression of
388 some ISGs including *Cxcl10*, *STAT1*, *Ifit1/2*, *Rsad2*, *Isg15,* and *Oasl2* (**S4 Fig**). In addition, the
389 inflammatory cytokine levels (*IL6*, *Tnf* and *Il27)* were comparable in both lungs and brain between
390 two groups (**Figure 5B and S4 Fig**). Interestingly, we found that humanized mice expressed
391 significantly higher levels of *Sele* (E-selectin) and *Selp* (P-selectin) in the brain, but not in the
392 lungs, indicating increased endothelial activation and inflammation in the brain of humanized mice
393 with *Ot* infection.
394

395 **Dysregulated innate and adaptive immune cell response in humanized mice following *Ot***
396 **infection**

397 *Ot* infection triggers robust innate and adaptive immune responses, characterized by strong type 1
398 immunity and activation of multiple immune cell subsets, including NK cells, macrophages,
399 dendritic cells, neutrophils, and effector T cells. While these cells play critical roles in controlling
400 bacterial replication and dissemination, their excessive activation can lead to
401 immunopathogenesis. We found that *Ot* infection induced stronger $CD4^+$ and $CD8^+$ T effector cell
402 responses in the spleens of humanized mice compared to WT controls (**Figure 6A**). However,
403 there was a significantly decreased percentage of Treg cells among $CD4^+$ T cells (**Figure 6B**).
404 Moreover, $CTLA4^+$ Treg cell numbers were markedly reduced in humanized mouse spleens
405 (**Figure 6C**). This result suggests that *Ot* infection leads to excessive T cell activation accompanied
406 by a diminished immunosuppressive T cell response in humanized mice.

407

408 **Excessive neutrophil response and limited innate immune cell activation in humanized mice**

409 Neutrophilia is observed in scrub typhus patients and is linked to disease progress(44, 45). We
410 found that infected humanized mice exhibited 3.4-fold higher neutrophil numbers in the spleen as
411 compared to WT controls (**Figure 7A**). Monocytes were also recruited into the spleen following
412 infection, with comparable infiltration levels observed between WT and humanized mice (**Figure**
413 **7B**). Notably, both macrophages and dendritic cells in infected humanized mice exhibited reduced
414 MHC II expression, indicating impaired activation of antigen-presenting cells in response to
415 human IFN-γ signaling. Humanized mice also harbored significantly fewer NK cells, which
416 displayed a markedly lower activation status, as evidenced by reduced CD69 expression (**Figure**

417 **7C**). Overall, our results suggest an increased neutrophil response alongside impaired activation
418 of other innate immune cells in humanized mice of *Ot* infection.
419
420 **Discussion**
421 Scrub typhus is a systemic, life-threatening disease with a high incidence in the "tsutsugamushi
422 triangle", yet it remains significantly neglected(46). A better understanding of *Ot* pathogenesis and
423 the development of effective vaccines represent the most promising strategies for preventing future
424 outbreaks of this disease(47, 48). Although several animal models have been established by other
425 researchers and our group(14-19, 21, 22, 28, 49, 50), there remains a need for an accurate mouse
426 model that closely recapitulates human scrub typhus. In this study, we introduce a newly developed
427 genetically engineered humanized mouse model for scrub typhus, featuring functional human IFN-
428 γ signaling in the absence of murine IFN-γ signaling. We demonstrated that this humanized mouse
429 strain exhibits increased susceptibility to intradermal *Ot* infection, characterized by multiorgan
430 bacterial dissemination, skin eschar formation, systemic inflammation, altered serum biochemical
431 profiles, and dysregulated innate and adaptive immune responses. This study represents the first
432 establishment of a scrub typhus model using genetically engineered humanized mice, and our
433 findings support the utility of this model as a promising tool for future studies on pathogenesis,
434 drug screening, and vaccine development.
435
436 We have previously demonstrated that IFN-γ signaling is necessary for host defense against *Ot*
437 infection as the *Ifngr1*$^{-/-}$ mouse strain, in contrast to WT B6 mice, develops a lethal model of scrub
438 typhus and forms a skin eschar lesion at the site of intradermal inoculation(25). The eschar serves
439 as a key diagnostic indicator in patients with acute febrile illness in regions endemic for scrub

440 typhus(51-53). Clinical observation indicates that the presence of an eschar might be associated
441 with increased disease severity(54, 55). Our study reports skin eschar lesions in an
442 immunocompetent mouse model in response to *Ot* infection for the first time. Representative HE
443 staining of eschar lesions show apparent immune infiltration in both humanized and *Ifngr1*$^{-/-}$ mice,
444 but not in WT mice (Figure 1E). Therefore, our data generated from our humanized mouse model
445 (Figure 1), along with the previously published *Ifngr1*$^{-/-}$ model(25) suggest that the species-specific
446 differences in IFN-γ signaling might be a critical determinant of eschar formation and disease
447 severity of scrub typhus. The downstream mechanisms by which IFN-γ signaling influences eschar
448 formation, however, still remain unclear. Interestingly, unlike mouse cells that express strong
449 inducible nitric oxide synthase (iNOS) by IFN-γ stimulation, human cells instead produce
450 indoleamine dioxygenase (34). Due to the key role of iNOS in wound healing(56), it is possible
451 that compromised IFN-γ/iNOS signaling contributes to eschar formation in not only scrub typhus,
452 but also rickettsial infection(57). Further studies are needed to elucidate downstream mechanisms
453 by which IFN-γ signaling influences eschar formation.
454
455 Scrub typhus can cause systemic infection and multiorgan dysfunction, particularly in cases with
456 delayed diagnosis and treatment. Immune infiltration in response to infection leads to
457 inflammatory damage and organ failure in patients(52, 58-60). Our histology assessment, serum
458 Bio-plex assay, biochemical analysis and bacterial burden measurement collectively demonstrate
459 systemic bacterial dissemination and inflammatory responses across multiple organs, including
460 lung, liver and brain in the humanized mouse model (Figure 2, 4 and 5). The immune and
461 biochemical profiles in humanized mice revealed unique features consistent with those observed
462 in our recently published *Ifngr1*$^{-/-}$ mouse model(25). For example, serum analysis revealed

463 elevated IL-6 in humanized mice compared to WT mice following infection, a characteristic that
464 is also noted in scrub typhus patients (61, 62). Similar IL-6 upregulation was also observed in
465 *Ifngr1*$^{-/-}$ mice infected with *Ot*(25), indicating that the proinflammatory cytokine IL-6 may serve
466 as a potential biomarker for predicting disease severity in scrub typhus. In addition, the decreased
467 serum levels of ALP, ALB and GLU which were found in infected *Ifngr1*$^{-/-}$ mice(25), were also
468 observed in humanized mice compared to WT controls (Figure 4), indicating excessive liver
469 dysfunction in this novel mouse model. Therefore, combining serum cytokine profiles and
470 biochemical parameters with bacterial load may offer a more accurate prediction of disease
471 severity in scrub typhus patients.
472
473 Scrub typhus has become a leading cause of central nervous system infection in endemic
474 regions(63, 64). Severe infection can lead to a range of neurological complications, including
475 meningitis, encephalitis, and meningoencephalitis, which are associated with increased
476 mortality(35, 41, 65-68). Moreover, *Ot* infection may increase the risk of long-term sequelae and
477 neurodegenerative diseases, such as dementia(69, 70). In this study, the increased susceptibility of
478 humanized mice to *Ot* infection is evidenced by higher bacterial burdens in multiple organs
479 compared to WT mice (Figure 5A). Notably, brain tissues of humanized mice exhibited the most
480 pronounced increase, with bacterial burdens approximately 10-fold higher than those in WT
481 controls. The uncontrolled bacterial replication observed in the brain may be attributed to the
482 substantial downregulation of several ISGs (Figure 5B). Consistent with this, histological analysis
483 also showed significant immune cell infiltration within the brain meninges of humanized mice,
484 which may contribute to meningoencephalitis (Figure 2). The significantly elevated expression of
485 key adhesion molecules *Sele* (E-selectin) and *Selp* (P-selectin) in the brains of humanized mice

486 may indicate robust neuroinflammation and potential blood-brain barrier dysfunction(71-73).
487 These findings may support the utility of the humanized mouse model as a valuable tool for
488 investigating neurological complications associated with scrub typhus.
489
490 We further evaluated innate and adaptive immune responses in humanized mice following
491 infection (Figure 5-7, S2 Fig and S3 Fig). Activation of IFN signaling induces robust expression
492 of ISGs, which play a critical role in controlling pathogen replication(74-76). Thus, we first
493 analyzed a comprehensive ISG expression panel in both the brain and lungs. We found that the
494 expression of several ISGs (*Ifit1*, *Ifit2, Rsad2, Isg15, Cxcl10* and *Oasl2*) were downregulated in
495 both organs of humanized mice, whereas members of the *Gbp* family (*Gbp2*, *Gbp4* and *Gbp5*),
496 were selectively reduced in the brain. Given that bacterial burdens in humanized mice were
497 approximately 10-fold higher in the brain and only 2.5-fold higher in the lungs compared to WT
498 mice (Figure 5A), these findings suggest that distinct ISGs may contribute differentially to
499 bacterial control in an organ specific manner. Next, we used flow cytometry to profile innate and
500 adaptive immune cell populations in the spleens. We observed an imbalance between effector and
501 regulatory T cells in humanized mice, characterized by an increase in activated effector T cells
502 and a reduction in Treg cells (Figure 6). This imbalance might be due to the impaired bacterial
503 clearance and may lead to heightened systemic inflammation. It is known that IFN signaling is
504 critical for antigen-presenting cell maturation and NK cell activation(77-80). Our data showed that
505 humanized IFN-γ signaling led to a significant reduction in MHC class II expression on antigen-
506 presenting cells and impaired activation of NK cells (Figure 7). This finding reveals a potential
507 underlying mechanism for the greater susceptibility of humans to *Ot* infection compared to mice.
508 Neutrophilia is a common feature of acute scrub typhus(44) and increased neutrophil activation

509 has been associated with disease progression(45). Consistent with these clinical observations, we
510 found that neutrophil populations were more than 3-fold higher in humanized mice compared to
511 WT mice following infection (Figure 7), suggesting that this humanized mouse model recapitulates
512 key aspects of immune dysregulation observed in patients with acute scrub typhus. Lastly, we
513 measured the *Ot*-specific antibody titers in mouse serum and found that humanized mice produced
514 IgM and IgG comparable to those of WT controls (S3 Fig). The intact antibody response supports
515 the suitability of this animal model for future vaccine studies.
516
517 Humanized mouse models represent promising tools for studying scrub typhus. Jiang et al. found
518 that humanized DRAGA mice were highly susceptible to intradermal and subcutaneous infection,
519 mounted strong $CD4^+$ and cytotoxic T cell responses, and produced human IgM and IgG following
520 repeated immunization, suggesting it as a new pre-clinical model for *Ot* pathogenesis study and
521 vaccine candidate testing(50). Our study using mice with humanized IFN-γ signaling builds on our
522 recent findings that IFN-γ, rather than type I interferons, plays a critical role in skin eschar
523 formation and host defense against *Ot* infection(25). To our knowledge, this triple KO/KI mouse
524 model has never been applied in any research study so far. Although the vendor validated the
525 genetic manipulation, downstream signaling activation, and immune cell profiles, we further
526 confirmed the expression of IFN-γ and its receptors in both humanized and WT mice during
527 infection (Figure 3). A limitation of our study is the limited number of animals available, which
528 restricted our ability to comprehensively assess the temporal dynamics of susceptibility, pathology,
529 and immune responses. Since our model is a genetically engineered humanized mouse strain, it
530 should not be confused with cellular humanization, where mice are engrafted with human cells
531 such as hematopoietic stem cells or peripheral blood mononuclear cells. Moreover, these germline-

532 modified mice can be bred, making them a more cost-effective and time-efficient option for
533 experimental studies.
534
535 In sum, we reported a novel humanized mouse model that is susceptible to *Ot* infection and forms
536 skin eschars via an intradermal infection route, effectively replicating human scrub typhus disease.
537 Future investigations are warranted by using this novel model to evaluate bacterial virulence,
538 characterize host protective immunity and assess the efficacy of potential new vaccine candidates.
539

540 **Acknowledgements**
541 We would like to thank the UTMB Flow Cytometry and Cell Sorting Core Lab (Meredith Weglarz)
542 and Dr. Joseph Jelinski for sample analysis and manuscript revision, respectively.
543

544 **Figure Legends**

545 **Figure 1. Humanized mice are susceptible to *Ot* infection.** WT B6 (n=6), *Ifngr1*$^{-/-}$ (n=4) and
546 humanized (n=4) mice were intradermally infected with *Ot* (3×10^3 FFU) on the right flank. Mice
547 were monitored daily for (A) body weight changes and (B) disease scores. (C) Skin eschar lesions
548 at inoculation sites at 11 dpi are presented and (D) their sizes are measured. (E) Representative
549 histological images of the skin eschar lesion are shown at 11 dpi. Scale bar = 100 μm. Data are
550 presented as mean ± SD from two independent pooled experiments. Body weight changes were
551 analyzed by two-way ANOVA with Tukey's multiple comparisons between WT and humanized
552 mice at indicated time points. Disease scores (11 and 14 dpi) and skin eschar lesion size (11 dpi)
553 were analyzed by one-way ANOVA with Tukey's multiple comparisons. *, $p < 0.05$; **, $p < 0.01$;
554 ***, $p < 0.001$; ****, $p < 0.0001$.

555

556 **Figure 2. Tissue histology of WT, *Ifngr1*$^{-/-}$ and humanized mice following *Ot* infection.** WT
557 B6 (n=9) and humanized (n=6) mice were infected as described in Figure 1. Uninfected WT B6
558 (n=3) and humanized (n=2) were i.d. injected with L929 cell culture control. Representative
559 histological images of the liver, lung and brain are shown at 14 dpi. Scale bar = 100 μm.

560

561 **Figure 3. Expression of *Ifng*, *Ifngr1* and *Ifngr2* in WT and humanized mice.** Mice were
562 infected as described in Figure 2. (A-B) RNA was extracted from mouse brain and lung tissues.
563 Mouse and human *Ifngr1* and *Ifngr2* transcript levels were analyzed by RT-qPCR, and the relative
564 fold changes are shown. (C) Human IFN-γ levels in the sera of WT B6 and humanized mice were
565 measured by sandwich ELISA. The label "u.d." represents undetectable levels. Data are presented
566 as mean ± SD from three independent pooled experiments.

567

568 **Figure 4. Serum cytokines and chemistry profiles in humanized mice with *Ot* infection.** Mice
569 were infected as described in Figure 1. (A) Serum cytokine and chemokine levels were analyzed
570 at 14 dpi by a Bio-Plex assay. (B) The serum chemistry parameters were detected by using VetScan
571 Comprehensive Diagnostic Profile Reagent Rotor. The parameters include alanine
572 aminotransferase (ALT), albumin (ALB), alkaline phosphatase (ALP), amylase (AMY), total
573 calcium (CA^{++}), globulin (GLOB), glucose (GLU), potassium (K^{+}), sodium (NA^{+}), total protein
574 (TP), blood urea nitrogen (BUN), and phosphorus (PHOS). Data are shown as mean ± SD from
575 three pooled independent experiments and analyzed by one-way ANOVA with a Tukey's multiple
576 comparisons test. *, $p < 0.05$; **, $p < 0.01$; ***, $p < 0.001$; ****, $p < 0.0001$.

577

578 **Figure 5. Humanized mice exhibited an increased bacterial burden and reduced expression**
579 **of interferon stimulated genes (ISGs) following *Ot* infection.** Mice were infected as described
580 in Figure 1 and were euthanized at 14 dpi. (A) Genomic DNA was isolated from the lung, spleen,
581 brain, kidney and liver. Bacterial burden was measured by qPCR. (B) The transcript levels of ISGs
582 in the brain were analyzed by qRT-PCR. Data are shown as mean ± SD from three pooled
583 independent experiments and analyzed by unpaired t-test for bacterial burdens and one-way
584 ANOVA with a Šídák's multiple comparisons test for ISG expression. *, $p < 0.05$; **, $p < 0.01$;
585 ***, $p < 0.001$; ****, $p < 0.0001$; ns, no significant difference.
586
587 **Figure 6. Imbalanced T cell responses in humanized mice following infection.** Mice were
588 infected as described in Figure 1 and were euthanized at 14 dpi. Spleen cells were isolated and
589 analyzed by flow cytometry. Single cells were gated first by FSC/SSC, followed by the exclusion
590 of dead cells by live/dead staining. (A-B) $CD4^+$ and $CD8^+$ T cells were gated on $CD3^+CD4^+$ and
591 $CD3^+CD8^+$, respectively. $CD44^+CD62L^-$ T cells were identified as activated populations. (C) For
592 regulatory T (Treg) cells, Foxp3 was gated on $CD4^+$ T cells and the expression of CTLA4 was
593 further gated on $CD4^+Foxp3^+$ T cells. The percentages of cell populations were shown as mean ±
594 SD on the flow cytometric images and the statistical analysis between infected WT and humanized
595 mice were labeled. The absolute numbers of cell populations were also calculated and shown next
596 to the flow cytometric images. One-way ANOVA with a Šídák's multiple comparisons test was
597 used for data analysis. *, $p < 0.05$; **, $p < 0.01$; ***, $p < 0.001$; ****, $p < 0.0001$.
598
599 **Figure 7. Excessive neutrophils and reduced innate immune cell activation in humanized**
600 **mice following *Ot* infection.** Mice were infected as described in Figure 1 and were euthanized at

601 14 dpi. Spleen cells were isolated and analyzed by flow cytometry. Single cells were gated first by
602 FSC/SSC, followed by the exclusion of dead cells by live/dead staining. (A-B) Neutrophils and
603 monocytes were identified by $CD11^{+}Ly6G^{+}$ and $CD11b^{+}Ly6C^{hi}$, respectively. $CD11b^{+}Ly6C^{-}$ cells
604 were further gated by CD11c and F4/80 markers. Macrophages and dendritic cells were
605 characterized by $CD11c^{-}F4/80^{+}$ and $CD11c^{hi}F4/80^{+}$, respectively. The mean fluorescent intensity
606 (MFI) of MHCII on macrophages and dendritic cells were measured. (C) NK cells were gated on
607 $CD3^{-}NK1.1^{+}$, and CD69 was used as an activation marker of NK cells. The percentages of cell
608 populations were shown as mean ± SD on the flow cytometric images and the statistical analysis
609 between infected WT and humanized mice were labeled. The absolute numbers and MFI of cell
610 populations were also calculated and were shown next to the flow cytometric images. One-way
611 ANOVA with a Šídák's multiple comparisons was used for data analysis. *, $p < 0.05$; **, $p < 0.01$;
612 ***, $p < 0.001$; ****, $p < 0.0001$.
613
614 **S1 Table. Sequences of PCR primers.** All primer sequences are obtained from PrimerBank
615 (https://pga.mgh.harvard.edu/primerbank/) or our previous publications.
616
617 **S2 Fig. Skin histology of uninfected mice.**
618 Skin tissues from uninfected WT and humanized mice were collected and subjected to H&E
619 staining. Representative histological images are shown at 14 dpi. Scale bar = 100 µm.
620
621 **S3 Fig. Comparable *Ot*-specific IgM and IgG levels in humanized and WT control mice.** To
622 measure relative amounts of IgM and IgG antibodies, mouse sera were collected at 14 dpi as shown
623 in Figure 1 and then diluted to create a dilution curve. Uninfected mouse sera were used as controls.

624 The area under the curve (AUC) is calculated from three pooled independent experiments and
625 shown as mean ± SD. One-way ANOVA with a Šídák's multiple comparisons was used for data
626 analysis. *, $p < 0.05$; **, $p < 0.01$.
627
628 **S4 Fig. Reduced expression of ISGs in the lungs of humanized mice with *Ot* infection.** Mice
629 were infected as described in Figure 1 and were euthanized at 14 dpi. The transcript levels of ISGs
630 and inflammatory genes in the lungs were analyzed by qRT-PCR. Data are shown as mean ± SD
631 from three pooled independent experiments and analyzed by one-way ANOVA with a Šídák's
632 multiple comparisons test. *, $p < 0.05$; **, $p < 0.01$; ***, $p < 0.001$.
633
634 **References**

635 1. Xu G, Walker DH, Jupiter D, Melby PC, Arcari CM. A review of the global epidemiology
636 of scrub typhus. PLoS Negl Trop Dis. 2017;11(11):e0006062.
637 2. Luce-Fedrow A, Lehman ML, Kelly DJ, Mullins K, Maina AN, Stewart RL, et al. A
638 Review of Scrub Typhus (*Orientia tsutsugamushi* and Related Organisms): Then, Now, and
639 Tomorrow. Trop Med Infect Dis. 2018;3(1):8.
640 3. Shin EH, Roh JY, Park WI, Song BG, Chang KS, Lee WG, et al. Transovarial transmission
641 of *Orientia tsutsugamushi* in Leptotrombidium palpale (Acari: Trombiculidae). PLoS One.
642 2014;9(4):e88453.
643 4. Venkategowda PM, Rao SM, Mutkule DP, Rao MV, Taggu AN. Scrub typhus: Clinical
644 spectrum and outcome. Indian J Crit Care Med. 2015;19(4):208-13.
645 5. Jeong YJ, Kim S, Wook YD, Lee JW, Kim KI, Lee SH. Scrub typhus: clinical, pathologic,
646 and imaging findings. Radiographics. 2007;27(1):161-72.

647 6. Taylor AJ, Paris DH, Newton PN. A Systematic Review of Mortality from Untreated Scrub
648 Typhus (*Orientia tsutsugamushi*). PLoS Negl Trop Dis. 2015;9(8):e0003971.
649 7. Peter JV, Sudarsan TI, Prakash JA, Varghese GM. Severe scrub typhus infection: Clinical
650 features, diagnostic challenges and management. World J Crit Care Med. 2015;4(3):244-50.
651 8. Pai H, Sohn S, Seong Y, Kee S, Chang WH, Choe KW. Central nervous system
652 involvement in patients with scrub typhus. Clin Infect Dis. 1997;24(3):436-40.
653 9. Kim DM, Kim SW, Choi SH, Yun NR. Clinical and laboratory findings associated with
654 severe scrub typhus. BMC Infect Dis. 2010;10:108.
655 10. Jiang J, Richards AL. Scrub Typhus: No Longer Restricted to the Tsutsugamushi Triangle.
656 Trop Med Infect Dis. 2018;3(1):11.
657 11. Chen K, Travanty NV, Garshong R, Crossley D, Wasserberg G, Apperson CS, et al.
658 Detection of *Orientia* spp. Bacteria in Field-Collected Free-Living *Eutrombicula* Chigger Mites,
659 United States. Emerg Infect Dis. 2023;29(8):1676-9.
660 12. Chaichana P, Satapoomin N, Kullapanich C, Chuenklin S, Mohammad A, Inthawong M,
661 et al. Comparative virulence analysis of seven diverse strains of *Orientia tsutsugamushi* reveals a
662 multifaceted and complex interplay of virulence factors responsible for disease. PLoS Pathog.
663 2025;21(6):e1012833.
664 13. Walker DH, Mendell NL. A scrub typhus vaccine presents a challenging unmet need. NPJ
665 Vaccines. 2023;8(1):11.
666 14. Mendell NL, Xu G, Shelite TR, Bouyer DH, Walker DH. A Murine Model of Waning
667 Scrub Typhus Cross-Protection between Heterologous Strains of *Orientia tsutsugamushi*.
668 Pathogens. 2022;11(5):512.

669 15. Luce-Fedrow A, Chattopadhyay S, Chan TC, Pearson G, Patton JB, Richards AL.
670 Comparison of Lethal and Nonlethal Mouse Models of *Orientia tsutsugamushi* Infection Reveals
671 T-Cell Population-Associated Cytokine Signatures Correlated with Lethality and Protection. Trop
672 Med Infect Dis. 2021;6(3):121.
673 16. Linsuwanon P, Wongwairot S, Auysawasdi N, Monkanna T, Richards AL, Leepitakrat S,
674 et al. Establishment of a Rhesus Macaque Model for Scrub Typhus Transmission: Pilot Study to
675 Evaluate the Minimal *Orientia tsutsugamushi* Transmission Time by Leptotrombidium
676 chiangraiensis Chiggers. Pathogens. 2021;10(8):1028.
677 17. Sunyakumthorn P, Somponpun SJ, Im-Erbsin R, Anantatat T, Jenjaroen K, Dunachie SJ,
678 et al. Characterization of the rhesus macaque (Macaca mulatta) scrub typhus model: Susceptibility
679 to intradermal challenge with the human pathogen *Orientia tsutsugamushi* Karp. PLoS Negl Trop
680 Dis. 2018;12(3):e0006305.
681 18. Mendell NL, Bouyer DH, Walker DH. Murine models of scrub typhus associated with host
682 control of *Orientia tsutsugamushi* infection. PLoS Negl Trop Dis. 2017;11(3):e0005453.
683 19. Soong L, Mendell NL, Olano JP, Rockx-Brouwer D, Xu G, Goez-Rivillas Y, et al. An
684 Intradermal Inoculation Mouse Model for Immunological Investigations of Acute Scrub Typhus
685 and Persistent Infection. PLoS Negl Trop Dis. 2016;10(8):e0004884.
686 20. Paris DH, Chattopadhyay S, Jiang J, Nawtaisong P, Lee JS, Tan E, et al. A nonhuman
687 primate scrub typhus model: protective immune responses induced by pKarp47 DNA vaccination
688 in cynomolgus macaques. J Immunol. 2015;194(4):1702-16.
689 21. Shelite TR, Saito TB, Mendell NL, Gong B, Xu G, Soong L, et al. Hematogenously
690 disseminated *Orientia tsutsugamushi*-infected murine model of scrub typhus [corrected]. PLoS
691 Negl Trop Dis. 2014;8(7):e2966.

692 22. Keller CA, Hauptmann M, Kolbaum J, Gharaibeh M, Neumann M, Glatzel M, et al.
693 Dissemination of *Orientia tsutsugamushi* and inflammatory responses in a murine model of scrub
694 typhus. PLoS Negl Trop Dis. 2014;8(8):e3064.
695 23. Ewing EP, Jr., Takeuchi A, Shirai A, Osterman JV. Experimental infection of mouse
696 peritoneal mesothelium with scrub typhus rickettsiae: an ultrastructural study. Infect Immun.
697 1978;19(3):1068-75.
698 24. Thiriot JD, Liang Y, Gonzales C, Sun J, Yu X, Soong L. Differential cellular immune
699 responses against *Orientia tsutsugamushi* Karp and Gilliam strains following acute infection in
700 mice. PLoS Negl Trop Dis. 2023;17(12):e0011445.
701 25. Liang Y, Wang H, Sun K, Sun J, Soong L. Lack of the IFN-gamma signal leads to lethal
702 *Orientia tsutsugamushi* infection in mice with skin eschar lesions. PLoS Pathog.
703 2024;20(5):e1012020.
704 26. Liang Y, Wang H, Gonzales C, Thiriot J, Sunyakumthorn P, Melby PC, et al.
705 CCR7/dendritic cell axis mediates early bacterial dissemination in *Orientia tsutsugamushi*-
706 infected mice. Front Immunol. 2022;13:1061031.
707 27. Petermann M, Orfanos Z, Sellau J, Gharaibeh M, Lotter H, Fleischer B, et al. CCR2
708 Deficiency Impairs Ly6C(lo) and Ly6C(hi) Monocyte Responses in *Orientia tsutsugamushi*
709 Infection. Front Immunol. 2021;12:670219.
710 28. Sunyakumthorn P, Paris DH, Chan TC, Jones M, Luce-Fedrow A, Chattopadhyay S, et al.
711 An intradermal inoculation model of scrub typhus in Swiss CD-1 mice demonstrates more rapid
712 dissemination of virulent strains of *Orientia tsutsugamushi*. PLoS One. 2013;8(1):e54570.

713 29. Munch CC, Upadhaya BP, Rayamajhee B, Adhikari A, Munch M, En-Nosse N, et al.
714 Multiple *Orientia* clusters and Th1-skewed chemokine profile: a cross-sectional study in patients
715 with scrub typhus from Nepal. Int J Infect Dis. 2023;128:78-87.
716 30. Inthawong M, Sunyakumthorn P, Wongwairot S, Anantatat T, Dunachie SJ, Im-Erbsin R,
717 et al. A time-course comparative clinical and immune response evaluation study between the
718 human pathogenic *Orientia tsutsugamushi* strains: Karp and Gilliam in a rhesus macaque (Macaca
719 mulatta) model. PLoS Negl Trop Dis. 2022;16(8):e0010611.
720 31. Fisher J, Card G, Liang Y, Trent B, Rosenzweig H, Soong L. *Orientia tsutsugamushi*
721 selectively stimulates the C-type lectin receptor Mincle and type 1-skewed proinflammatory
722 immune responses. PLoS Pathog. 2021;17(7):e1009782.
723 32. Soong L, Wang H, Shelite TR, Liang Y, Mendell NL, Sun J, et al. Strong type 1, but
724 impaired type 2, immune responses contribute to *Orientia tsutsugamushi*-induced pathology in
725 mice. PLoS Negl Trop Dis. 2014;8(9):e3191.
726 33. Schroder K, Hertzog PJ, Ravasi T, Hume DA. Interferon-gamma: an overview of signals,
727 mechanisms and functions. J Leukoc Biol. 2004;75(2):163-89.
728 34. Roshick C, Wood H, Caldwell HD, McClarty G. Comparison of gamma interferon-
729 mediated antichlamydial defense mechanisms in human and mouse cells. Infect Immun.
730 2006;74(1):225-38.
731 35. Liang Y, Aditi, Onyoni F, Wang H, Gonzales C, Sunyakumthorn P, et al. Brain
732 transcriptomics reveal the activation of neuroinflammation pathways during acute *Orientia*
733 *tsutsugamushi* infection in mice. Front Immunol. 2023;14:1194881.

734 36. Giengkam S, Blakes A, Utsahajit P, Chaemchuen S, Atwal S, Blacksell SD, et al. Improved
735 Quantification, Propagation, Purification and Storage of the Obligate Intracellular Human
736 Pathogen *Orientia tsutsugamushi*. PLoS Negl Trop Dis. 2015;9(8):e0004009.
737 37. Liang Y, Fisher J, Gonzales C, Trent B, Card G, Sun J, et al. Distinct Role of TNFR1 and
738 TNFR2 in Protective Immunity Against *Orientia tsutsugamushi* Infection in Mice. Front Immunol.
739 2022;13:867924.
740 38. Trent B, Liang Y, Xing Y, Esqueda M, Wei Y, Cho NH, et al. Polarized lung inflammation
741 and Tie2/angiopoietin-mediated endothelial dysfunction during severe *Orientia tsutsugamushi*
742 infection. PLoS Negl Trop Dis. 2020;14(3):e0007675.
743 39. Gonzales C, Liang Y, Fisher J, Card G, Sun J, Soong L. Alterations in germinal center
744 formation and B cell activation during severe *Orientia tsutsugamushi* infection in mice. PLoS Negl
745 Trop Dis. 2023;17(5):e0011090.
746 40. Dittrich S, Sunyakumthorn P, Rattanavong S, Phetsouvanh R, Panyanivong P,
747 Sengduangphachanh A, et al. Blood-Brain Barrier Function and Biomarkers of Central Nervous
748 System Injury in Rickettsial Versus Other Neurological Infections in Laos. Am J Trop Med Hyg.
749 2015;93(2):232-7.
750 41. Alam AM, Gillespie CS, Goodall J, Damodar T, Turtle L, Vasanthapuram R, et al.
751 Neurological manifestations of scrub typhus infection: A systematic review and meta-analysis of
752 clinical features and case fatality. PLoS Negl Trop Dis. 2022;16(11):e0010952.
753 42. Moron CG, Popov VL, Feng HM, Wear D, Walker DH. Identification of the target cells of
754 *Orientia tsutsugamushi* in human cases of scrub typhus. Mod Pathol. 2001;14(8):752-9.
755 43. Platanias LC. Mechanisms of type-I- and type-II-interferon-mediated signalling. Nat Rev
756 Immunol. 2005;5(5):375-86.

757 44. Cho BA, Ko Y, Kim YS, Kim S, Choi MS, Kim IS, et al. Phenotypic characterization of
758 peripheral T cells and their dynamics in scrub typhus patients. PLoS Negl Trop Dis.
759 2012;6(8):e1789.
760 45. Paris DH, Stephan F, Bulder I, Wouters D, van der Poll T, Newton PN, et al. Increased
761 Nucleosomes and Neutrophil Activation Link to Disease Progression in Patients with Scrub
762 Typhus but Not Murine Typhus in Laos. PLoS Negl Trop Dis. 2015;9(8):e0003990.
763 46. Walker DH. Scrub Typhus - Scientific Neglect, Ever-Widening Impact. N Engl J Med.
764 2016;375(10):913-5.
765 47. Banerjee A, Kulkarni S. *Orientia tsutsugamushi*: The dangerous yet neglected foe from the
766 East. Int J Med Microbiol. 2021;311(1):151467.
767 48. Valbuena G, Walker DH. Approaches to vaccines against *Orientia tsutsugamushi*. Front
768 Cell Infect Microbiol. 2012;2:170.
769 49. Thiriot J, Liang Y, Fisher J, Walker DH, Soong L. Host transcriptomic profiling of CD-1
770 outbred mice with severe clinical outcomes following infection with *Orientia tsutsugamushi*. PLoS
771 Negl Trop Dis. 2022;16(11):e0010459.
772 50. Jiang L, Morris EK, Aguilera-Olvera R, Zhang Z, Chan TC, Shashikumar S, et al.
773 Dissemination of *Orientia tsutsugamushi*, a Causative Agent of Scrub Typhus, and Immunological
774 Responses in the Humanized DRAGA Mouse. Front Immunol. 2018;9:816.
775 51. Kundavaram AP, Jonathan AJ, Nathaniel SD, Varghese GM. Eschar in scrub typhus: a
776 valuable clue to the diagnosis. J Postgrad Med. 2013;59(3):177-8.
777 52. Paris DH, Phetsouvanh R, Tanganuchitcharnchai A, Jones M, Jenjaroen K, Vongsouvath
778 M, et al. *Orientia tsutsugamushi* in human scrub typhus eschars shows tropism for dendritic cells
779 and monocytes rather than endothelium. PLoS Negl Trop Dis. 2012;6(1):e1466.

780 53. Park J, Woo SH, Lee CS. Evolution of Eschar in Scrub Typhus. Am J Trop Med Hyg.
781 2016;95(6):1223-4.
782 54. Sonthayanon P, Chierakul W, Wuthiekanun V, Phimda K, Pukrittayakamee S, Day NP, et
783 al. Association of high *Orientia tsutsugamushi* DNA loads with disease of greater severity in adults
784 with scrub typhus. J Clin Microbiol. 2009;47(2):430-4.
785 55. Chauhan V, Thakur A, Thakur S. Eschar is associated with poor prognosis in scrub typhus.
786 Indian J Med Res. 2017;145(5):693-6.
787 56. Kitano T, Yamada H, Kida M, Okada Y, Saika S, Yoshida M. Impaired Healing of a
788 Cutaneous Wound in an Inducible Nitric Oxide Synthase-Knockout Mouse. Dermatol Res Pract.
789 2017;2017:2184040.
790 57. Anh Phuong Luu AAG, Alexis Bouin, Nir Drayman, Thomas P. Burke. Differences
791 between human and rodent nitric oxide production dictate susceptibility to tick-borne Rickettsia.
792 bioRxiv [Preprint]. 2025 Jun 29:2025.06.27.661835.
793 58. Hsu YH, Chen HI. Pulmonary pathology in patients associated with scrub typhus.
794 Pathology. 2008;40(3):268-71.
795 59. Chauhan R, Ahmad S, Goyal C, Tewatia P. Hepatopathy in Scrub Typhus: Clinical
796 Presentation, Association With Morbidity and Impact on Outcome. Cureus. 2024;16(1):e52316.
797 60. Neyaz Z, Bhattacharya V, Muzaffar N, Gurjar M. Brain MRI findings in a patient with
798 scrub typhus infection. Neurol India. 2016;64(4):788-92.
799 61. Chung DR, Lee YS, Lee SS. Kinetics of inflammatory cytokines in patients with scrub
800 typhus receiving doxycycline treatment. J Infect. 2008;56(1):44-50.

801 62. Paris DH, Chansamouth V, Nawtaisong P, Lowenberg EC, Phetsouvanh R, Blacksell SD,
802 et al. Coagulation and inflammation in scrub typhus and murine typhus--a prospective comparative
803 study from Laos. Clin Microbiol Infect. 2012;18(12):1221-8.
804 63. Pulla P. Disease sleuths unmask deadly encephalitis culprit. Science. 2017;357(6349):344.
805 64. Mittal M, Thangaraj JWV, Rose W, Verghese VP, Kumar CPG, Mittal M, et al. Scrub
806 Typhus as a Cause of Acute Encephalitis Syndrome, Gorakhpur, Uttar Pradesh, India. Emerg
807 Infect Dis. 2017;23(8):1414-6.
808 65. Basu S, Chakravarty A. Neurological Manifestations of Scrub Typhus. Curr Neurol
809 Neurosci Rep. 2022;22(8):491-8.
810 66. Garg D, Manesh A. Neurological Facets of Scrub Typhus: A Comprehensive Narrative
811 Review. Ann Indian Acad Neurol. 2021;24(6):849-64.
812 67. Fisher J, Card G, Soong L. Neuroinflammation associated with scrub typhus and spotted
813 fever group rickettsioses. PLoS Negl Trop Dis. 2020;14(10):e0008675.
814 68. Soong L, Shelite TR, Xing Y, Kodakandla H, Liang Y, Trent BJ, et al. Type 1-skewed
815 neuroinflammation and vascular damage associated with *Orientia tsutsugamushi* infection in mice.
816 PLoS Negl Trop Dis. 2017;11(7):e0005765.
817 69. Prakash Gangwar S, Thangaraj JWV, Zaman K, Vairamani V, Mittal M, Murhekar M.
818 Sequelae Following Acute Encephalitis Syndrome Caused by *Orientia Tsutsugamushi*. Pediatr
819 Infect Dis J. 2020;39(5):e52-e4.
820 70. Kim J, Seok H, Jeon JH, Choi WS, Seo GH, Park DW. Association of scrub typhus with
821 incidence of dementia: a nationwide population-based cohort study in Korea. BMC Infect Dis.
822 2023;23(1):127.

823 71. Paris DH, Jenjaroen K, Blacksell SD, Phetsouvanh R, Wuthiekanun V, Newton PN, et al.
824 Differential patterns of endothelial and leucocyte activation in 'typhus-like' illnesses in Laos and
825 Thailand. Clin Exp Immunol. 2008;153(1):63-7.
826 72. Tantibhedhyangkul W, Matamnan S, Longkunan A, Boonwong C, Khowawisetsut L.
827 Endothelial Activation in *Orientia tsutsugamushi* Infection Is Mediated by Cytokine Secretion
828 From Infected Monocytes. Front Cell Infect Microbiol. 2021;11:683017.
829 73. Sporn LA, Lawrence SO, Silverman DJ, Marder VJ. E-selectin-dependent neutrophil
830 adhesion to Rickettsia rickettsii-infected endothelial cells. Blood. 1993;81(9):2406-12.
831 74. Schoggins JW. Interferon-Stimulated Genes: What Do They All Do? Annu Rev Virol.
832 2019;6(1):567-84.
833 75. Schneider WM, Chevillotte MD, Rice CM. Interferon-stimulated genes: a complex web of
834 host defenses. Annu Rev Immunol. 2014;32:513-45.
835 76. Manful EE, Pietersen RD, Baker B. IFIT2-induced transcriptomic changes in
836 Mycobacterium tuberculosis infected macrophages. Front Cell Infect Microbiol.
837 2025;15:1536446.
838 77. Lin Q, Rong L, Jia X, Li R, Yu B, Hu J, et al. IFN-gamma-dependent NK cell activation is
839 essential to metastasis suppression by engineered *Salmonella*. Nat Commun. 2021;12(1):2537.
840 78. Horowitz A, Stegmann KA, Riley EM. Activation of natural killer cells during microbial
841 infections. Front Immunol. 2012;2:88.
842 79. Bian Y, Walter DL, Zhang C. Efficiency of Interferon-gamma in Activating Dendritic Cells
843 and Its Potential Synergy with Toll-like Receptor Agonists. Viruses. 2023;15(5):1198.
844 80. Schoenborn JR, Wilson CB. Regulation of interferon-gamma during innate and adaptive
845 immune responses. Adv Immunol. 2007;96:41-101.

846

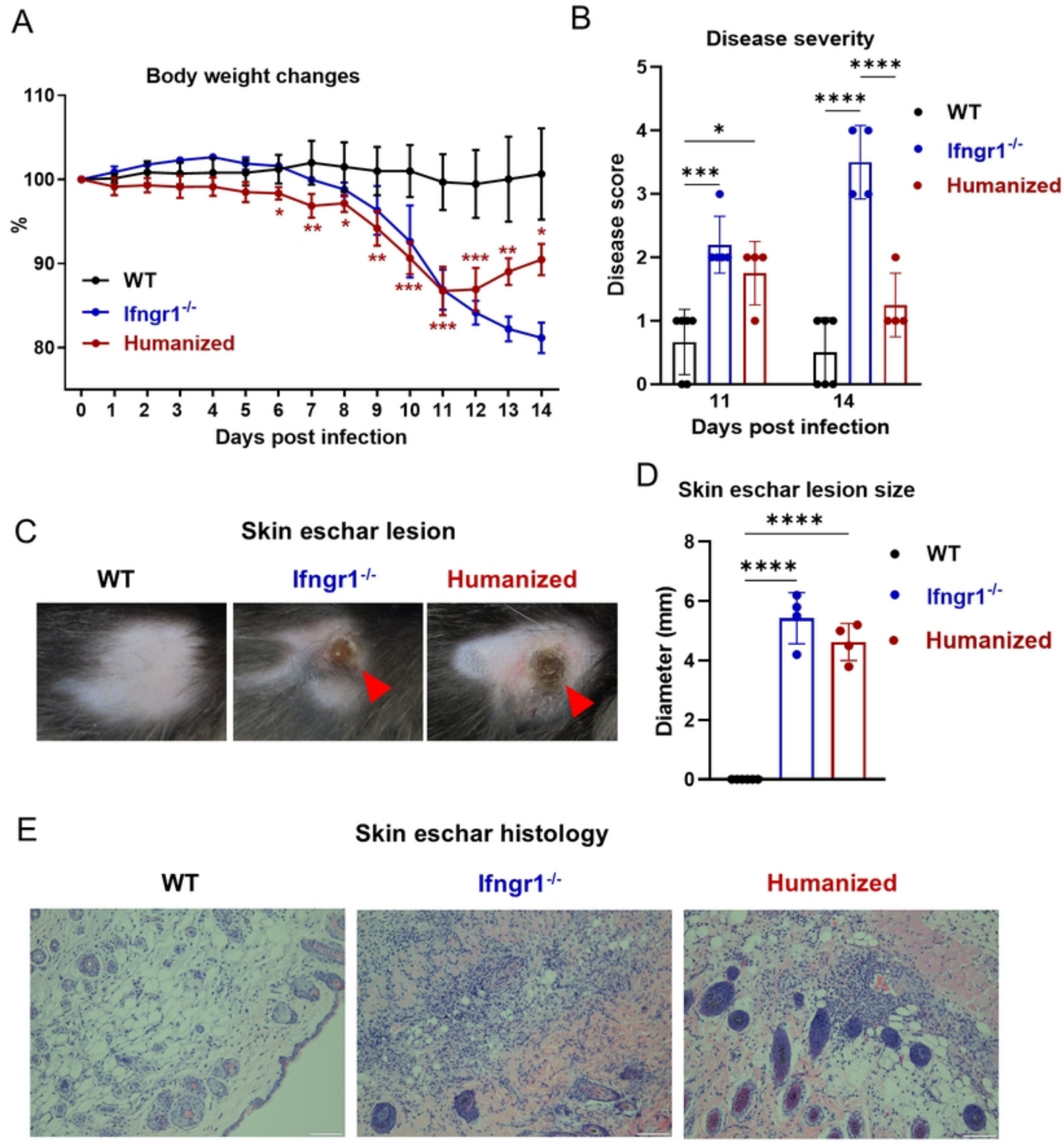
A
Body weight changes
110
100
90
80
%
WT
Ifngr1-/-
Humanized
0 1 2 3 4 5 6 7 8 9 10 11 12 13 14
Days post infection
B
Disease severity
Disease score
5
4
3
2
1
0
11
14
Days post infection
WT
Ifngr1-/-
Humanized
C
Skin eschar lesion
WT
Ifngr1-/-
Humanized
D
Skin eschar lesion size
Diameter (mm)
8
6
4
2
0
WT
Ifngr1-/-
Humanized
E
Skin eschar histology
WT
Ifngr1-/-
Humanized

Fig 1

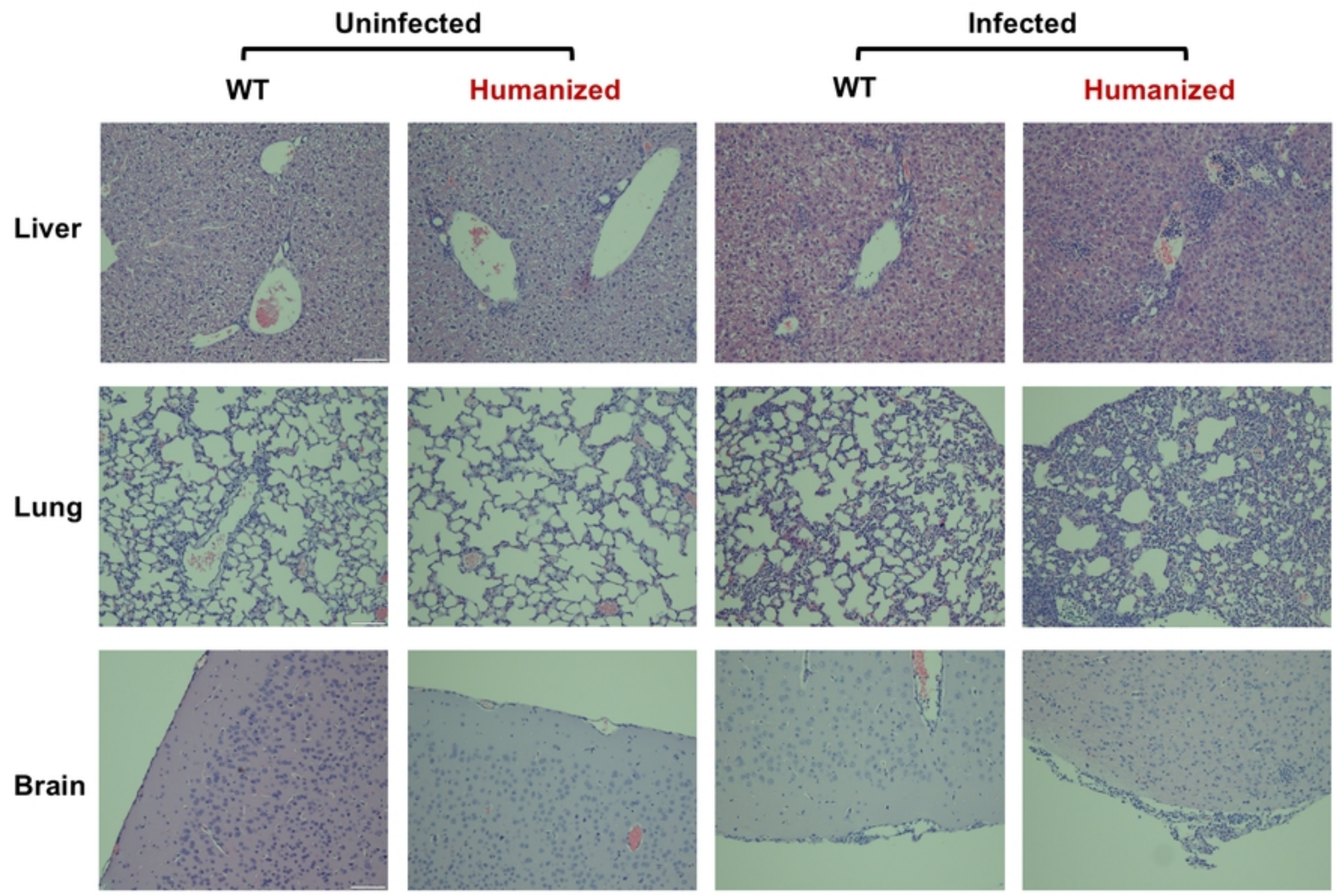
Uninfected
Infected
WT
Humanized
WT
Humanized
Liver
Lung
Brain

Fig 2

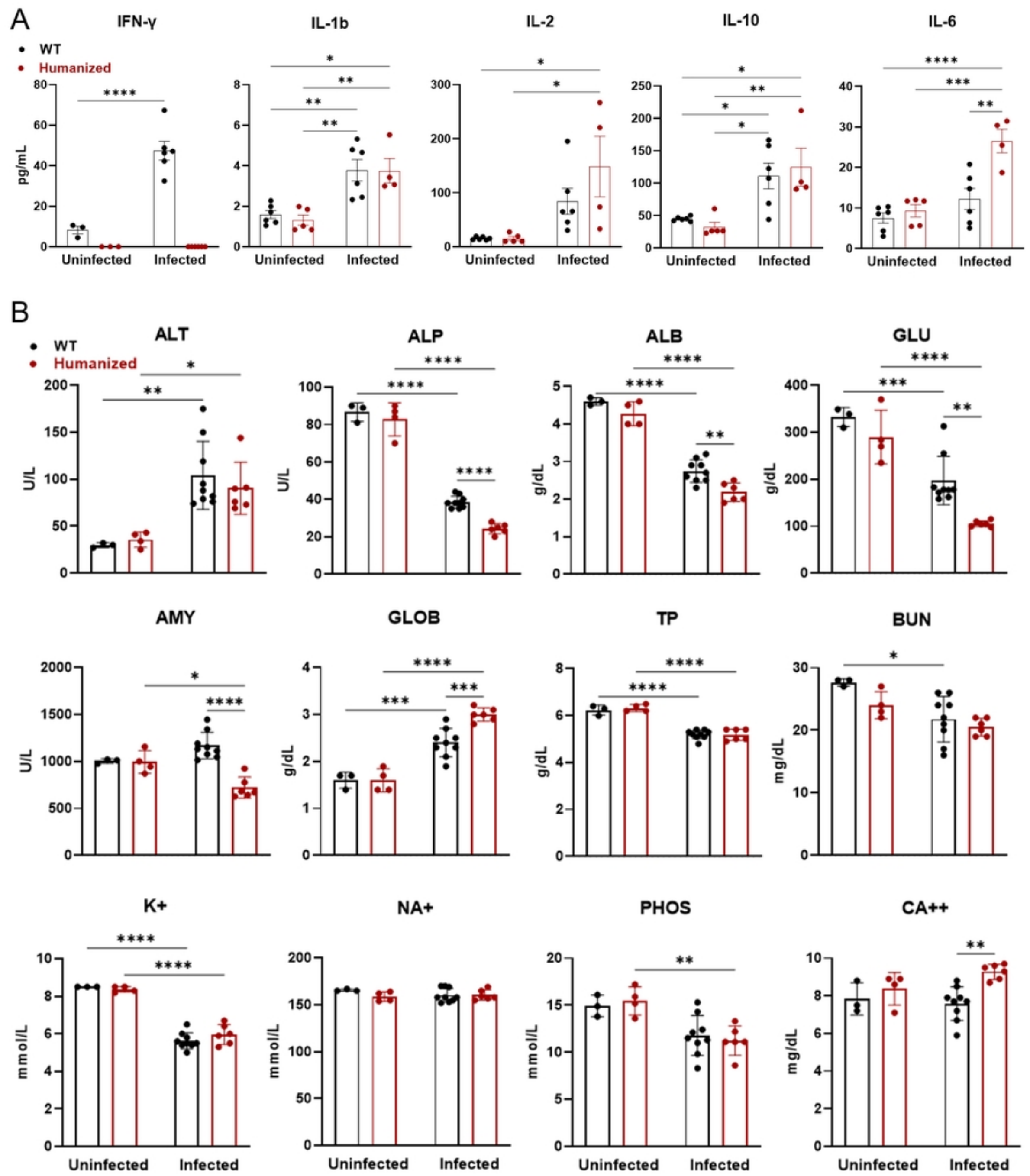
A
IFN-γ
IL-1b
IL-2
IL-10
IL-6
WT
Humanized
pg/mL
Uninfected
Infected
B
ALT
ALP
ALB
GLU
AMY
GLOB
TP
BUN
K+
NA+
PHOS
CA++
U/L
g/dL
mg/dL
mmol/L

Fig 4

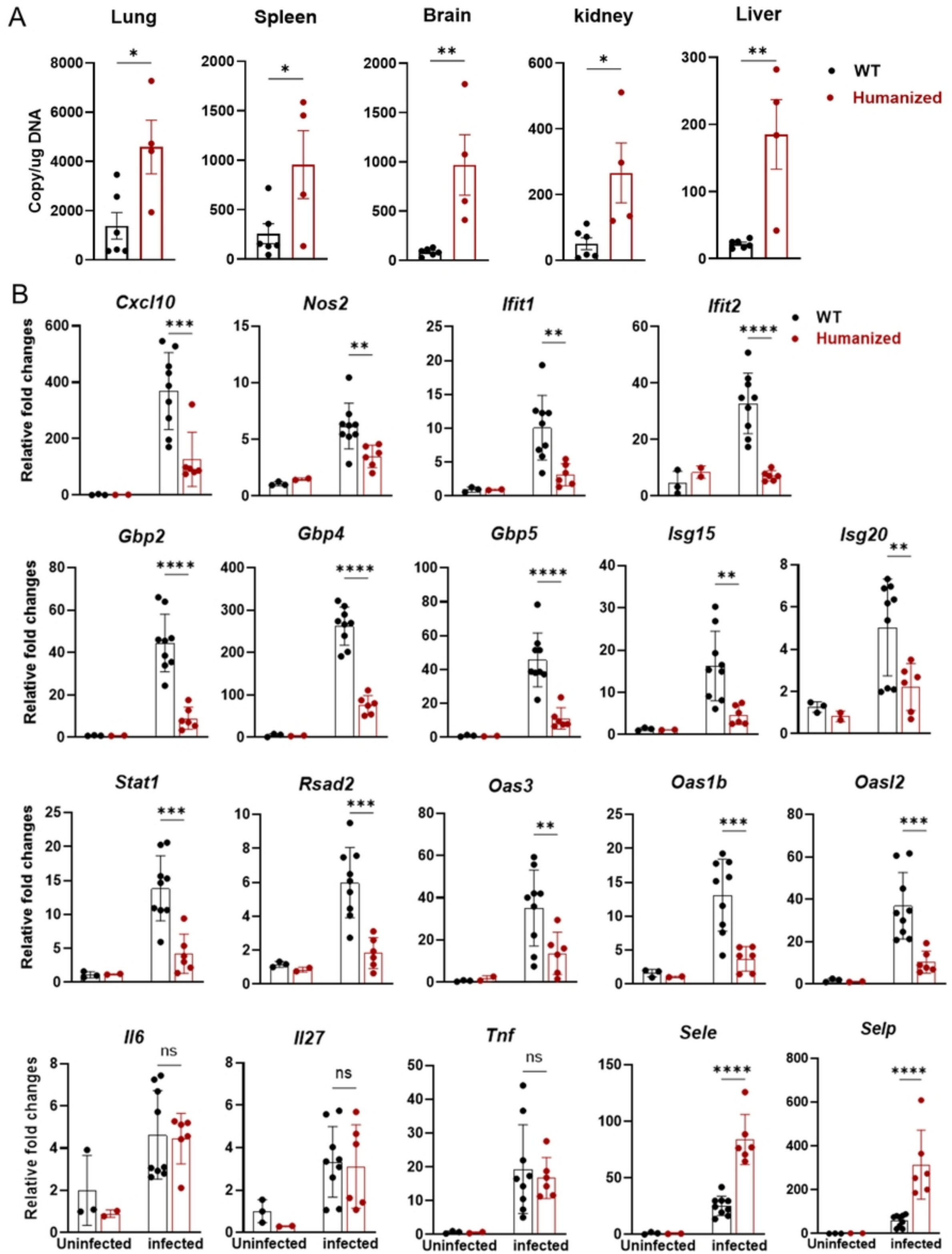
A
Lung
Spleen
Brain
kidney
Liver
Copy/ug DNA
WT
Humanized
B
Cxcl10
Nos2
Ifit1
Ifit2
Gbp2
Gbp4
Gbp5
Isg15
Isg20
Stat1
Rsad2
Oas3
Oas1b
Oasl2
Il6
Il27
Tnf
Sele
Selp
Relative fold changes
Uninfected
infected
ns

Fig 5

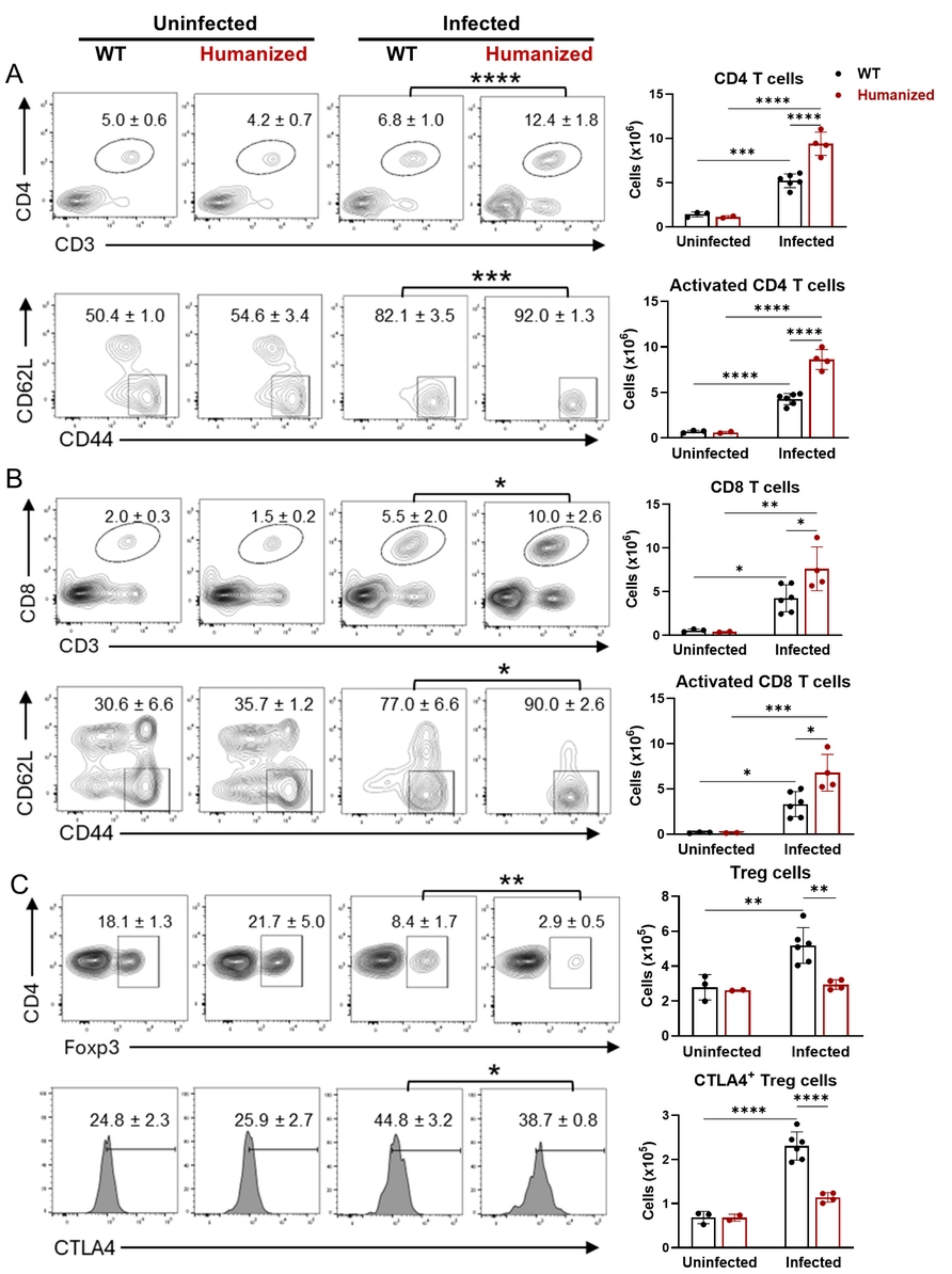
Uninfected
Infected
WT
Humanized
WT
Humanized
A
CD4
CD3
5.0 ± 0.6
4.2 ± 0.7
6.8 ± 1.0
12.4 ± 1.8
****
CD4 T cells
WT
Humanized
Cells (x10^6)
Uninfected
Infected
CD62L
CD44
50.4 ± 1.0
54.6 ± 3.4
82.1 ± 3.5
92.0 ± 1.3
***
Activated CD4 T cells
B
CD8
CD3
2.0 ± 0.3
1.5 ± 0.2
5.5 ± 2.0
10.0 ± 2.6
*
CD8 T cells
CD62L
CD44
30.6 ± 6.6
35.7 ± 1.2
77.0 ± 6.6
90.0 ± 2.6
Activated CD8 T cells
C
CD4
Foxp3
18.1 ± 1.3
21.7 ± 5.0
8.4 ± 1.7
2.9 ± 0.5
**
Treg cells
Cells (x10^5)
CTLA4
24.8 ± 2.3
25.9 ± 2.7
44.8 ± 3.2
38.7 ± 0.8
CTLA4+ Treg cells

Fig 6

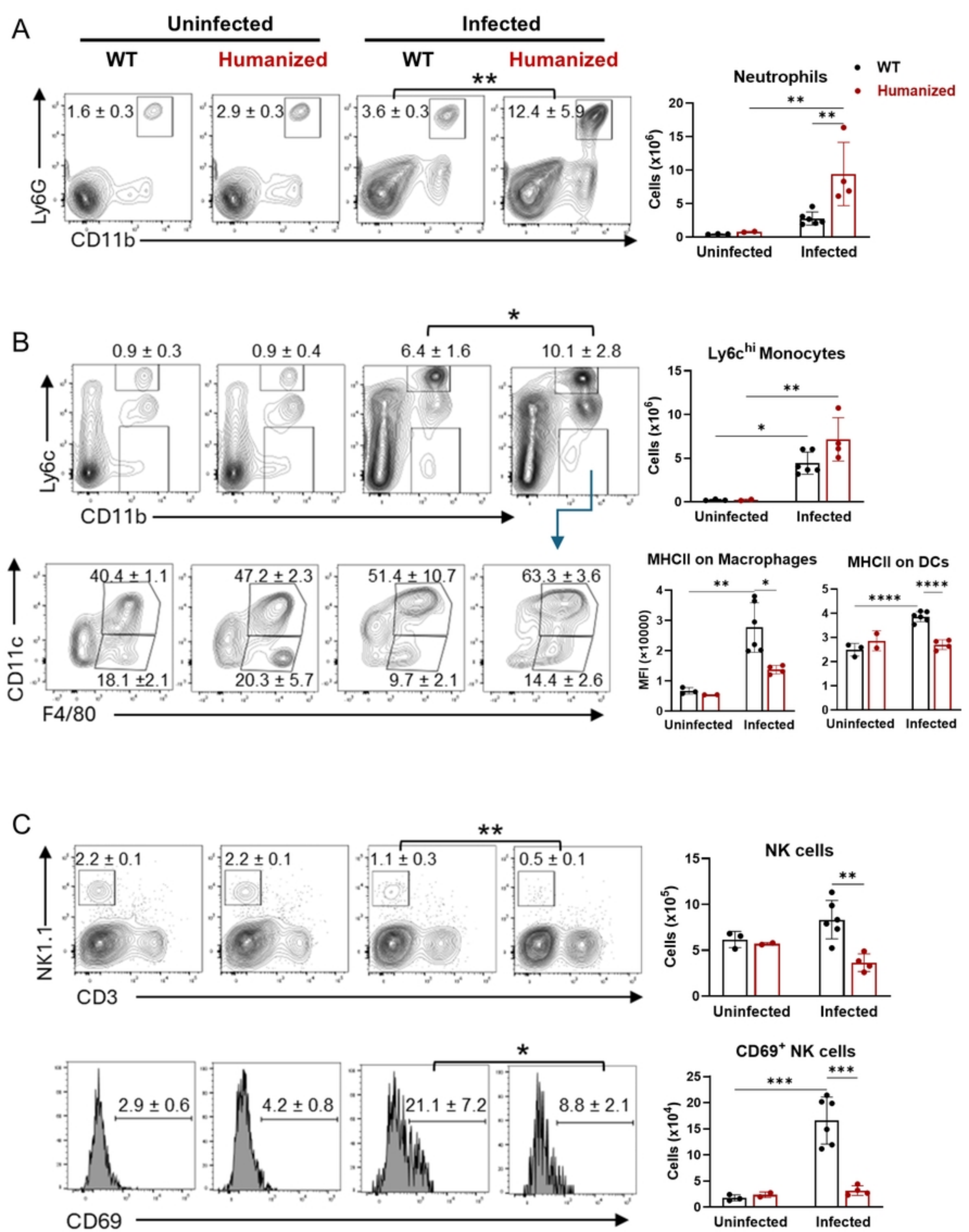
A
Uninfected
Infected
WT
Humanized
WT
Humanized
**
1.6 ± 0.3
2.9 ± 0.3
3.6 ± 0.3
12.4 ± 5.9
Ly6G
CD11b
Neutrophils
WT
Humanized
Cells (x10^6)
Uninfected
Infected
B
*
0.9 ± 0.3
0.9 ± 0.4
6.4 ± 1.6
10.1 ± 2.8
Ly6c
CD11b
Ly6c^hi Monocytes
Cells (x10^6)
Uninfected
Infected
40.4 ± 1.1
47.2 ± 2.3
51.4 ± 10.7
63.3 ± 3.6
18.1 ±2.1
20.3 ± 5.7
9.7 ± 2.1
14.4 ± 2.6
CD11c
F4/80
MHCII on Macrophages
MFI (×10000)
Uninfected
Infected
MHCII on DCs
Uninfected
Infected
C
**
2.2 ± 0.1
2.2 ± 0.1
1.1 ± 0.3
0.5 ± 0.1
NK1.1
CD3
NK cells
Cells (x10^5)
Uninfected
Infected
*
2.9 ± 0.6
4.2 ± 0.8
21.1 ± 7.2
8.8 ± 2.1
CD69
CD69+ NK cells
Cells (x10^4)
Uninfected
Infected

Fig 7

A

Brain

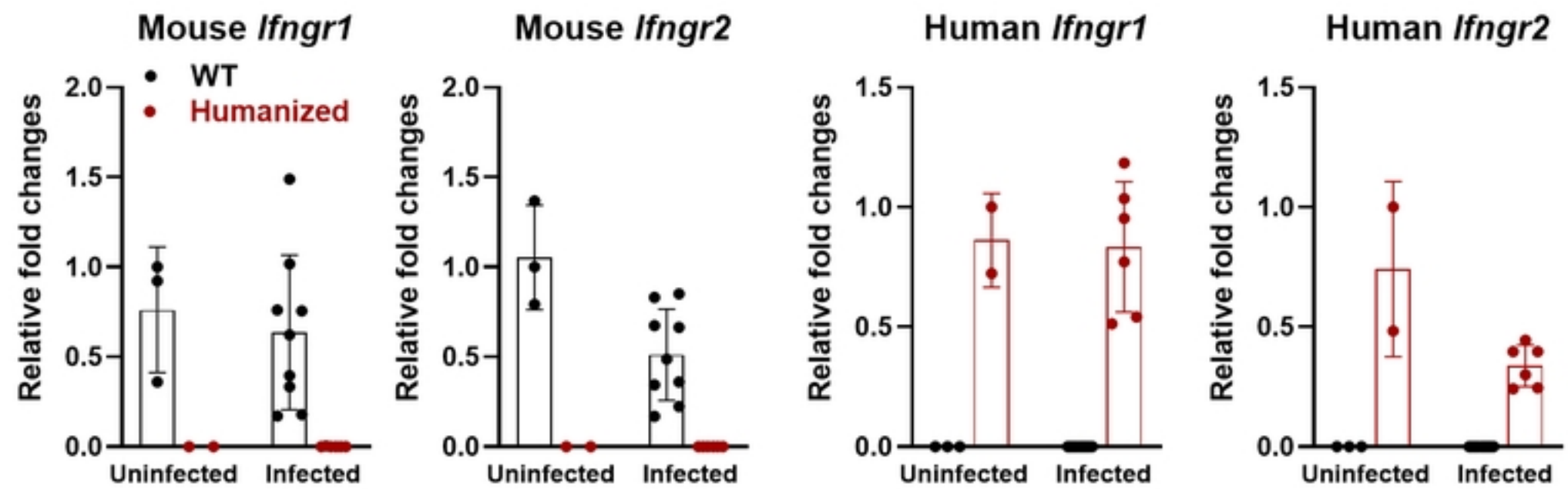

B

Lung

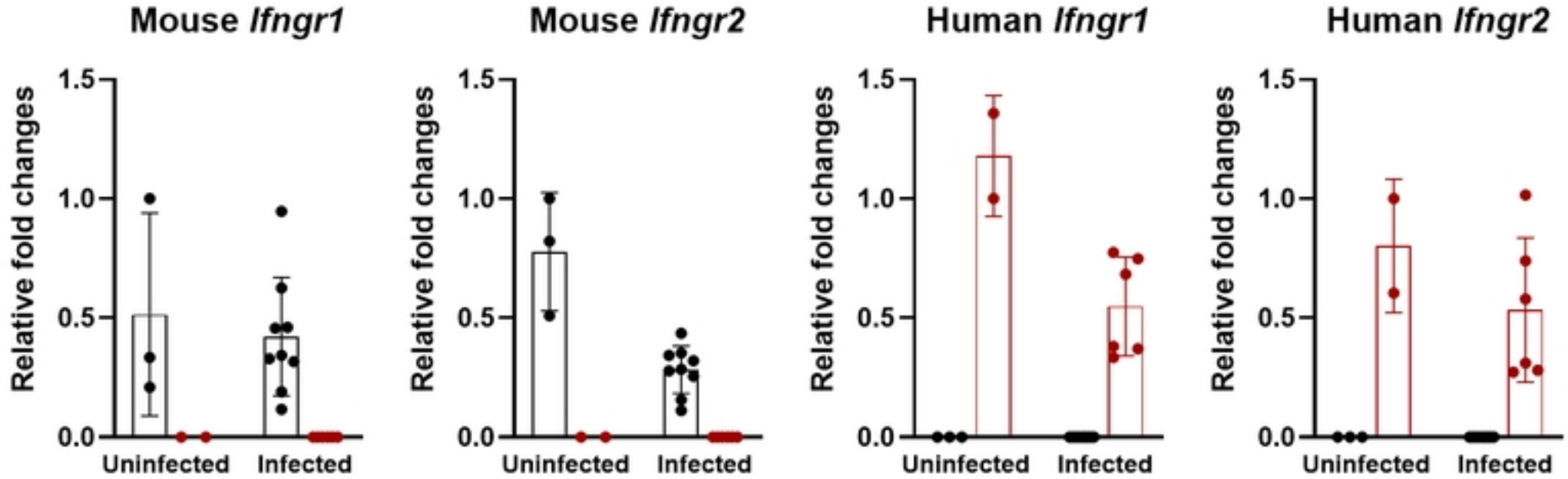

C

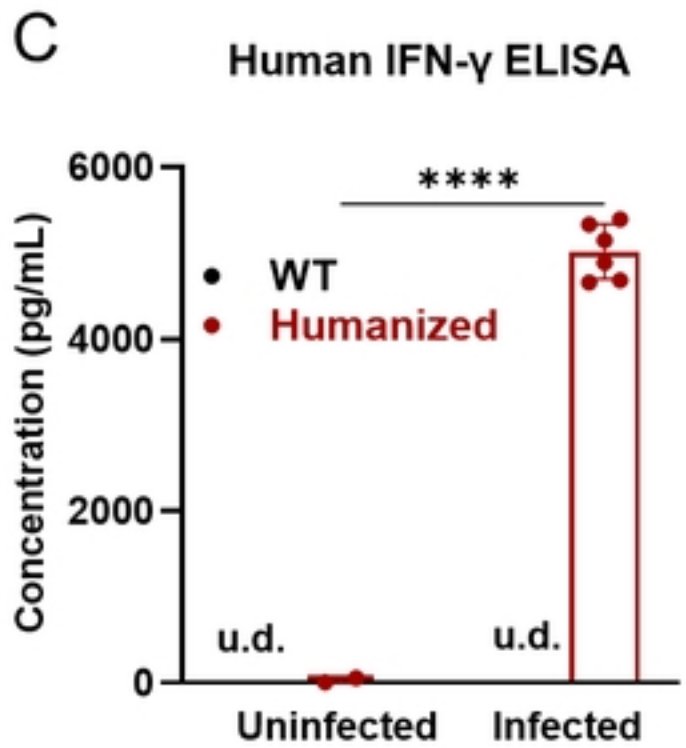

Fig 3